Research Square

Preprints are preliminary reports that have not undergone peer review.
They should not be considered conclusive, used to inform clinical practice,
or referenced by the media as validated information.

A Calcium-Releasing Graphene Oxide Transwell Interface for Bidirectional Electrochemical Oxygen Sensing of Epidermal Differentiation

Tae-Hyung Kim
thkim0512@skku.edu

Sungkyunkwan University
Cheol-Hwi Kim
Sungkyunkwan University
Fu Nan Ju
Chung-Ang University
Yun-Sik Eom
Sungkyunkwan University
Jin-Kyu Wi
Sungkyunkwan University
Chang-Dae Kim
Sungkyunkwan University

Article

Keywords:

Posted Date: July 1st, 2026

DOI: https://doi.org/10.21203/rs.3.rs-9987375/v1

License: This work is licensed under a Creative Commons Attribution 4.0 International License.
Read Full License

Additional Declarations: There is no conflict of interest

Abstract

Epidermal differentiation involves coordinated structural and metabolic remodeling, yet it is typically evaluated by endpoint molecular or imaging assays that cannot track the same culture over time. Here, we developed a graphene oxide–gelatin–calcium (GO-Gel-Ca) film-integrated transwell platform with bidirectional electrochemical sensing to track differentiation-associated oxygen dynamics in keratinocyte (HaCaT) cultures. The dissolvable film, composed of GO, gelatin, and calcium chloride, transiently sealed the polycarbonate membrane pores and provided gradual calcse, reopening the pores during culture to enable basal medium supply under air-liquid interface conditions. This interface reduced irregular HaCaT aggregation and promoted more spatially uniform differentiation than Gel-Ca and control membranes. Immunocytochemistry and RT-qPCR confirmed sequential induction of Keratin 10, involucrin, and filaggrin, with filaggrin increasing ~ 60-fold by 72 h. Using a sandwich-type bidirectional differential pulse voltammetry (DPV) configuration, oxygen-related responses were monitored from both the apical and basal sides of the cell-bearing membrane. The apical oxygen depletion rate underwent a positive-to-negative transition between 48 and 72 h, exceeding the basal depletion index at 48 h (63.9% versus 37.7%), whereas the basal transition was delayed beyond 72 h. This apical-leading, basal-lagging asymmetry resolved the spatial directionality of stratification non-destructively, distinguishing localized differentiation from global metabolic change. This information is inaccessible to conventional single-sided or endpoint assays. To our knowledge, this is the first electrochemical platform to capture such direction-dependent oxygen dynamics across a stratifying epithelium within an intact culture. This bidirectional electrochemical approach establishes a route to non-destructive, spatially resolved monitoring of epithelial maturation, opening opportunities for functional skin modeling, differentiation toxicology, and barrier-formation studies.

1. Introduction

The epidermis is a stratified epithelial barrier that protects against dehydration, pathogens, and environmental insults[1–4]. Its barrier function arises from progressive differentiation, in which proliferative basal keratinocytes withdraw from the cell cycle, acquire suprabasal phenotypes, and ultimately contribute to the cornified layer[5–7]. Because aberrant keratinocyte differentiation underlies impaired barrier function, inflammatory skin disorders, and defective wound repair, in vitro models that faithfully reproduce and quantitatively report epidermal maturation are essential not only for fundamental skin biology but also for predictive in vitro toxicology and regenerative skin engineering[8–11].

Current readouts of keratinocyte differentiation, however, remain largely endpoint-based. Immunostaining, PCR, western blotting, and histology yield rich molecular information but require fixation or lysis[12–14]. Consequently, time-dependent keratinization is reconstructed from independent samples rather than tracked within the same culture. Label-free alternatives such as transepithelial electrical resistance (TEER), impedance spectroscopy, and extracellular flux analysis (Seahorse XF) only partially address this gap[15,16]. Each is constrained by limited specificity to early differentiation,

morphology dependence, or incompatibility with repeated in situ measurement inside transwell-based air–liquid interface (ALI) architectures[17,18]. A further limitation is structural. HaCaT cultures compact unevenly as calcium-dependent adhesion strengthens during differentiation, producing local variations in cell density, layer thickness, and diffusion distance. These geometric variations distort any readout that integrates over the sensing interface[19–21].

Among candidate functional signals, oxygen dynamics provide a particularly informative readout, because epidermal differentiation is accompanied by pronounced metabolic remodeling[22,23]. Basal keratinocytes rely predominantly on glycolysis, whereas commitment is marked by a transient increase in mitochondrial respiration that subsequently declines as terminal cornification proceeds through organelle clearance and metabolic shutdown[24–26]. This stage-dependent shift produces a characteristic, time-resolved oxygen-consumption signature[27–30]. Electrochemical detection of dissolved oxygen is well suited for capturing these dynamics[31–34]. It is label-free, rapid, and compatible with repeated in situ acquisition. The measured current, however, reflects oxygen dynamics only in the immediate vicinity of the sensing interface[35–37]. It is shaped by cellular metabolism, local oxygen availability, cell-layer thickness, aggregation, membrane geometry, pore accessibility, and diffusion pathways[38,39]. Two design requirements follow. First, the culture interface must constrain structural heterogeneity so that signals are dominated by cellular rather than geometric variability. Second, the sensing scheme must resolve, rather than average over, the spatial directionality of oxygen depletion across a stratifying epithelium.

Here we report a transwell culture system modified with a graphene oxide–gelatin–calcium chloride (GO-Gel-Ca) film that simultaneously constrains structural heterogeneity and resolves directional oxygen depletion across a stratifying epithelium (Fig. 1). The platform integrates three co-designed components. First, the GO-Gel-Ca film acts as a sacrificial pore-gating interface on the polycarbonate membrane. GO reinforces the gelatin matrix and tunes its dissolution kinetics, gelatin supports initial keratinocyte attachment, and embedded calcium chloride provides sustained calcium availability to drive differentiation[40–44]. As the film dissolves, the membrane pores reopen to enable basal medium supply under ALI conditions, providing a more uniform culture geometry while preserving stratification. Second, a sandwich-type, apical–basal dual-electrode differential pulse voltammetry (DPV) configuration resolves direction-dependent oxygen depletion rate (ODR) profiles. This bidirectional readout separates localized differentiation-associated oxygen dynamics from generalized metabolic suppression, complementing conventional single-sided oxygen sensing. Third, because the GO-Gel-Ca film and the dual-electrode configuration share a common geometry, the uniform pore-gating imposed by the film ensures that the directional DPV-ODR signals reflect cellular rather than structural variability. Together, these elements provide a non-destructive, time-resolved, and direction-resolved readout of keratinocyte differentiation in transwell-based skin models.

2. Results and discussion

2.1. GO-Gel-Ca Film Fabrication

Calcium drives the basal-to-suprabasal transition during keratinocyte differentiation, but abrupt exposure to elevated calcium can induce ER stress, oxidative stress, or transient cytotoxicity that confounds the interpretation of differentiation markers such as involucrin and TGM1[45–48]. To enable gradual and spatially controlled calcium delivery, we developed a GO-gelatin film that incorporates calcium chloride and releases it as the film dissolves (Fig. 2). The relative composition of each component was tuned to control film dissolution and calcium release kinetics.

The GO-Gel-Ca film was fabricated by spin-coating a suspension of GO, gelatin, and calcium chloride onto a porous polycarbonate membrane (0.8 μm pores) at 500 rpm. The concentrations of GO and calcium chloride were fixed at 10 mg/mL and 1.6 mM, respectively, while the gelatin concentration was varied (Fig. 2a, 2b). The rheological analysis of the suspensions showed that the sample containing 10% gelatin exhibited a viscosity of 173 mPa·s at 600 s, whereas the suspension containing 0.1% gelatin showed a markedly lower viscosity of 1.7 mPa·s (Fig. 2c), governing coating morphology on the polycarbonate substrate. All formulations exhibited film-forming capability sufficient to seal the membrane pores. However, films with ≥ 5% gelatin showed pronounced shrinkage during drying, reduced uniformity, and partial detachment of pore-sealing regions, whereas 0.1% gelatin yielded minimal structural defects without observable shrinkage (Fig. 2d, Figure S1). Raman mapping based on the D/G band ratio confirmed the spatially uniform presence of GO throughout the coated regions, including pore-sealing zones (Fig. 2e, Figure S2). The D/G ratio, which reflects the relative abundance of sp^3 defect sites versus sp^2 graphitic domains, remained elevated across the sealed pores, indicating that the oxidized functional groups of GO were preserved during film formation, a prerequisite for calcium coordination at the film–water interface.

Calcium ions were retained and released through interactions with the GO and gelatin matrix[49]. GO carries abundant oxygen-containing functional groups (e.g., epoxy, carboxyl, carbonyl, and hydroxyl) on its basal plane and edge regions. These negatively charged groups can electrostatically coordinate calcium ions, contributing to calcium immobilization within the film[50]. SEM-EDS mapping confirmed the spatial co-localization of carbon, oxygen, and calcium signals on the as-prepared film (Fig. 2f, top row, Figure S3–S4). Following 72-h medium exposure, the calcium signal was no longer detectable, while the carbon and oxygen distributions remained essentially unchanged (Fig. 2f, bottom row). This selective loss of calcium against an intact GO–gelatin matrix directly visualizes the release of immobilized calcium without bulk degradation of the polymer–GO scaffold during this time window.

Unlike gelatin, film-formed GO layers do not readily dissolve in aqueous environments. Water penetration can induce interlayer swelling and partial destabilization of stacked GO structures, but complete disruption typically requires substantial hydration-assisted weakening or mechanical perturbation[51,52]. Gelatin, in contrast, rapidly swells and loses structural integrity upon hydration[49]. Combining GO with gelatin therefore enabled temporal regulation of film dissolution and calcium release. Dissolution under cell culture–like conditions was quantified through the reduction of pore-sealing regions. GO-sealed pores exhibited fluorescence quenching across a broad spectral range, consistent with the intrinsic

optical properties of GO; pore regions inducing fluorescence interference at 532 nm were therefore monitored as a proxy for residual sealing (Fig. 2g). The proportion of fluorescence-quenching pores decreased progressively with incubation time, indicating gradual film dissolution and reopening of the underlying membrane pores (Fig. 2h).

To resolve calcium release directionality, the GO-Gel-Ca film was integrated into a transwell system and analyzed independently from the insert-facing and well-facing surfaces. Inductively coupled plasma optical emission spectroscopy (ICP-OES) revealed cumulative calcium concentrations on the insert-facing side of 3.86, 13.68, 22.56, and 36.38 mg/L at 12, 24, 36, and 48 h, respectively, with strong linearity ($R^2 = 0.9786$) (Fig. 2i, Figure S5). At 72 h, the insert-facing concentration reached 47.1 mg/L, corresponding to approximately 78.5% of the incorporated calcium. In contrast, the well-facing side reached only ~ 3.3 mg/L at 72 h, approximately 15-fold lower than the insert-facing concentration (Fig. 2i). Notably, the well-facing release plateaued between 24 and 36 h (Fig. 2i, n.s.), suggesting that diffusion-mediated transport through the pores reached a quasi-steady state once the apical reservoir of released calcium was largely depleted. This pronounced directionality reflects the localization of the coating layer on the insert-facing surface and the diffusion-limited transport through the membrane pores, and supports the use of the GO-Gel-Ca film as a directionally controlled calcium-delivery interface. Distilled water was used for ICP-OES quantification, so the resulting profile should be interpreted as a controlled release trend rather than an exact representation of calcium availability in serum-containing culture medium.

2.2. Image-Based Monitoring of Keratinocyte Differentiation under Different Culture Conditions

The GO-Gel-Ca film was designed as a cartridge-type module that could be readily attached to and detached from the bottom of a customized transwell insert. When combined with a conventional well plate, this configuration enabled the establishment of an air-liquid interface (ALI) culture environment for keratinocytes (Fig. 3a). After an initial submerged culture period, ALI culture was initiated by exposing the apical side of the keratinocyte layer to air while maintaining medium supply from the basal compartment. This configuration allowed the GO-Gel-Ca film to function as both a calcium-delivery interface and a culture-supporting module.

To evaluate the differentiation-inducing performance of the film, four conditions were compared: bare polycarbonate membrane (control), gelatin-coated film, Gel-Ca film, and GO-Gel-Ca film (Fig. 3b, 3c). Keratin 14 (K14) was used as a basal/proliferative marker, and Keratin 10 (K10) as an early suprabasal differentiation marker. Marker-positive fluorescence regions were quantified using image-based post-processing — background correction, binary thresholding, and pixel-based area analysis — and the resulting fluorescence-positive area (FPA) was compared under identical image-processing conditions (Fig. 3c, Figure S6–S7). At 24 h, the uncoated control and gelatin-coated films showed limited K10-positive FPA (3,535 ± 670 and 3,440 ± 855 px, respectively), whereas the calcium-containing groups exceeded 26,840 ± 3,316 px, confirming that extracellular calcium availability is required for early

differentiation marker expression. As summarized schematically (Fig. 3a, right), films lacking GO showed enhanced cellular aggregation, heterogeneous differentiation areas, and non-uniform calcium supply, whereas the GO-Gel-Ca film suppressed aggregation and supported spatially uniform differentiation with sustained calcium release.

After 24 h of culture, all groups except the submerged control were exposed to ALI conditions. ALI-exposed groups showed markedly increased K10 expression, indicating transition from a proliferative state toward an early suprabasal phenotype. The gelatin-coated and GO-Gel-Ca films exhibited significant increases in K10-positive FPA after ALI exposure, whereas the Gel-Ca film showed only a limited difference before and after ALI exposure, a difference closely linked to the presence of GO in the film matrix. Calcium immobilization via the oxygen-containing functional groups of GO, demonstrated in Section 2.1, reduced abrupt burst release from the film. The GO-containing coating also supported more uniform cell distribution, likely through altered surface wettability, protein adsorption, and cell–substrate interactions, suppressing irregular cell aggregation after ALI exposure. Colony size distribution analysis confirmed that HaCaT colonies on the GO-Gel-Ca film were more spatially controlled than those on the Gel-Ca film (Figure S8). In contrast, the Gel-Ca film without GO exhibited burst calcium release within the initial exposure period (Figure S9); the resulting non-uniform calcium availability likely contributed to heterogeneous differentiation and disrupted the temporal sequence of marker expression.

Time-resolved immunostaining revealed that ALI exposure at 24 h triggered rapid K10 induction by 48 h on both gelatin and GO-Gel-Ca films, but only the GO-Gel-Ca group subsequently progressed to robust filaggrin expression at 72 h (Fig. 3b). As shown in Fig. 3c, the Gel-Ca film exhibited a gradual increase in K10 over time but with high variability in FPA, partly reflecting irregular cell aggregation and partly reflecting the effects of abrupt calcium exposure. The disproportionate elevation of filaggrin relative to K10 in the Gel-Ca group at 48 h further supports this interpretation: because keratinocyte differentiation proceeds sequentially, abrupt calcium exposure may bypass the canonical temporal order, triggering premature activation of late differentiation programs. In contrast, the GO-Gel-Ca group exhibited a temporally ordered differentiation profile. Quantitative FPA analysis showed that, at 48 h, K14, K10, and filaggrin FPAs on the GO-Gel-Ca film were 19.7, 62.5, and 16.7 ($\times 10^3$ px), respectively, and by 72 h reached 19.5, 64.7, and 70.8 ($\times 10^3$ px), with filaggrin showing the largest relative gain (Fig. 3c). Additionally, the coefficients of variation (CVs) of the FPAs differed markedly between the Gel-Ca and GO-Gel-Ca groups. For the K14, K10, and filaggrin FPAs at 72 h, the GO-Gel-Ca group exhibited lower CV values than the Gel-Ca group, suggesting that sample-to-sample variability in marker expression was reduced in the GO-Gel-Ca group. These image-based observations were corroborated by RT-qPCR (Fig. 3d, Figure S10): on the GO-Gel-Ca film, K10 transcript peaked at 48 h and decreased at 72 h, while involucrin and filaggrin transcripts increased monotonically to ~ 11- and ~ 6-fold by 72 h, respectively, consistent with progression from early suprabasal to advanced differentiation. Comparison across all four conditions highlighted the distinct roles of calcium and GO. Gelatin alone supported early K10 induction but yielded low involucrin and filaggrin, indicating arrest at early suprabasal stages. Adding calcium (Gel-Ca) elevated late markers but with disrupted temporal ordering. Only the full GO-Gel-Ca composition achieved sequential induction of K10, involucrin, and filaggrin (Fig. 3d). Collectively, the GO-

Gel-Ca film established a temporally controlled and spatially uniform calcium microenvironment under ALI conditions. This environment suppressed irregular aggregation, reduced spatial heterogeneity of marker expression, and supported sequential keratinocyte differentiation (Figure S11).

2.3. Estimation of Keratinocyte Differentiation Based on Oxygen Consumption Rate Monitoring

To obtain a reference metabolic profile for interpreting the differentiation-associated oxygen dynamics, we measured the oxygen consumption rate (OCR) and extracellular acidification rate (ECAR) of HaCaT cultures on Gel-Ca and GO-Gel-Ca films by Seahorse XF analysis (Fig. 4a–c). Total OCR is confounded by cell density, proliferation, and the glycolysis-biased metabolism of proliferating keratinocytes[53]. OCR was therefore interpreted alongside culture duration and the marker data of Section 2.2 rather than as a stand-alone differentiation index. At 24 h, OCR profiles were variable on both films and proton leak was elevated (8.6 ± 7.3 and 14.1 ± 2.3 pmol O_2/min for Gel-Ca and GO-Gel-Ca, respectively). This pattern is consistent with incomplete mitochondrial coupling during early attachment, so these provisional values were excluded from differentiation analysis.

The two films diverged sharply in the directionality of their respiratory trajectories, and this contrast was the most discriminating metabolic feature (Fig. 4d–f). On the Gel-Ca film, basal respiration and ATP production increased monotonically with time, while proton leak remained unresolved (Fig. 4e, n.s.). This signature reflects the continued accumulation of metabolically active, proliferative basal-type cells rather than terminal differentiation, in agreement with the disrupted marker ordering reported in Section 2.2. In contrast, the GO-Gel-Ca film showed a progressive decline in basal respiration, ATP production, and proton leak, with maximal respiration peaking at 48 h before decreasing (Fig. 4f). The resolution of proton leak toward near-zero by 72 h (2.5 ± 0.3 pmol O_2/min) was absent on Gel-Ca, indicating stabilization of mitochondrial coupling as differentiation advanced.

ECAR resolved the timing of this transition. Glycolytic activity on the GO-Gel-Ca film peaked sharply at 48 h (24.6 ± 6.3 mpH/min) and declined by 72 h (17.3 ± 8.8 mpH/min), whereas Gel-Ca increased monotonically. The 48 h glycolytic peak coincides with the K10 transcript maximum (Section 2.2), defining the early-suprabasal commitment window. Its subsequent decay, together with the falling respiration and resolving proton leak, describes a coherent energy arc on the GO-Gel-Ca film that the proliferation-like Gel-Ca profile lacks.

RT-qPCR confirmed that these changes were mitochondrially regulated (Fig. 4g–i). On the GO-Gel-Ca film, both MT-CO1 (complex IV) and TFAM (mitochondrial biogenesis) peaked at 48 h, reaching 8.7- and 3.5-fold increases, respectively, and then declined significantly by 72 h (4.3- and 2-fold, respectively). This reproduced, at the transcriptional level, the 48 h-peaked, 72 h-declining pattern of functional respiration. Gel-Ca did not recapitulate this coordinated peak-then-decline (MT-CO1, n.s. from 48 to 72 h), confirming that the ordered mitochondrial down-regulation is specific to the GO-Gel-Ca condition. Crucially, caspase 3 remained near baseline in all groups, with no significant change from 48 to 72 h (Fig. 4i, GO-Gel-Ca n.s.), excluding apoptosis as the cause of the late OCR decline. The g–i panels are

therefore internally consistent with the flux data, establishing the GO-Gel-Ca respiratory decline as a regulated, biogenesis-coupled feature of differentiation rather than a viability artifact.

The respiratory trajectories are best understood as a culture-stage program comprising an early attachment phase and two metabolically distinct differentiation phases[54]. During the initial attachment phase (0–24 h), incomplete mitochondrial coupling and unstable, low ATP-linked respiration reflect substrate adhesion and adaptation rather than differentiation, and were therefore excluded from analysis. In the commitment phase (~ 48 h on the GO-Gel-Ca film), keratinocytes engage both glycolytic and oxidative metabolism as they exit the proliferative state and enter early suprabasal differentiation. This is a transitional window in which peak glycolytic ECAR, maximal respiration, MT-CO1/TFAM expression, and the K10 transcript maximum converge. The pattern is consistent with the established proliferation-to-differentiation metabolic transition, in which glycolysis-biased basal keratinocytes progressively engage mitochondrial oxidative phosphorylation upon commitment[55,56]. In the terminal phase (~ 72 h), cornification proceeds. As keratinocytes lose their nuclei and mitochondria through regulated organelle clearance and become metabolically inactive, respiration, ATP production, proton leak, and mitochondrial transcripts decline in concert[57]. The absence of caspase 3 induction confirms that this reflects genuine keratinization rather than apoptotic death[58,59].

Critically, only the GO-Gel-Ca film progressed into this terminal phase, whereas the Gel-Ca film remained in the commitment phase. This divergence is the metabolic counterpart of the calcium-release behavior established in Sections 2.1–2.2: the sustained, GO-mediated calcium supply preserves the physiological differentiation sequence, whereas the burst release from the Gel-Ca film disrupts it and allows proliferative basal-type cells to keep accumulating, manifesting here as the monotonic rise in OCR and ECAR[60]. The metabolic trajectories thus provide an independent, function-level confirmation of the same mechanism inferred from film chemistry and marker imaging.

In summary, the GO-Gel-Ca film supports a complete, stage-ordered metabolic program of keratinization. Oxidative commitment at 48 h is followed by cornification-associated mitochondrial down-regulation at 72 h, whereas the burst-calcium Gel-Ca film arrests at the proliferative-commitment stage. This directional contrast, corroborated by concordant MT-CO1/TFAM regulation and the absence of caspase 3 induction, identifies GO-Gel-Ca as the condition that most faithfully recapitulates ordered keratinocyte differentiation. Seahorse analysis is, however, destructive, requires dissociation from the ALI architecture, and lacks spatial directionality. This metabolic reference therefore anchors the interpretation of the bidirectional DPV-ODR measurements, which uniquely provide the non-destructive, in situ, direction-resolved oxygen readout described in the following section.

2.4. Estimation of Keratinocyte Differentiation Based on Bidirectional Electrochemical Oxygen Depletion Monitoring

The metabolic remodeling that accompanies keratinocyte differentiation (Section 2.3) is reflected in extracellular oxygen dynamics, which can be read non-destructively by electrochemistry. We therefore

developed a bidirectional DPV-based strategy that tracks the cathodic current of oxygen reduction from both the apical and basal sides of the culture interface. This current scales with the dissolved oxygen remaining near the electrode after cellular consumption, as confirmed by oxygen-sensitivity calibration, providing a functional, label-free readout that preserves the culture structure[61,62].

The GO-Gel-Ca film was integrated into an assembly-type cartridge positioned between two identically configured gold nanostructure–deposited working electrodes, each with its own reference and counter electrodes for independent apical and basal monitoring (Fig. 5a–b, Figure S12). The detection solution (HBSS) was nitrogen-purged to a consistent baseline and calibrated to 61 ± 0.5 μA at − 0.3 V (Figure S13); currents were analyzed as absolute peak values. A cell density–dependent analysis showed that the response varied with cell number near the interface, confirming the cell-dependent origin of the signal (Figure S14). Because two opposing directions are recorded, the signals capture not only total oxygen consumption but also directional differences in oxygen transport and cell-layer organization.

The apical DPV signal decreased steeply up to 48 h, indicating progressively increasing oxygen depletion during proliferation and early differentiation (Fig. 5c, 5d, Figure S15–S16). The basal side followed a comparable trend only to 24 h, where the two directions were similar (apical 44 ± 2.33, basal 41 ± 0.81 μA; n.s.). At 48 h, the directions diverged: the apical signal fell to a minimum of ~ 22 μA, whereas the basal rate of decrease slowed markedly (Figure S17). Beyond 48 h, both signals partially recovered—apical to ~ 33 μA by 72 h and basal to ~ 45 μA by 120 h—indicating a reversal toward reduced net oxygen depletion at later stages. This recovery is unlikely to reflect sensor drift, since the two directions recover with different magnitudes and timing. Instead, it is consistent with the combined effect of declining mitochondrial oxygen demand and an increasing diffusion barrier as the keratinocyte layer stratifies and keratinizes, a regime in which the upper, air-exposed layers are known to become progressively oxygen-limited.

To quantify these dynamics, DPV responses were converted into an oxygen depletion index (ODI), defined as the relative decrease in signal from baseline (Fig. 5e):

$$\text{Oxygen depletion index (ODI)} = \frac{\mathrm{I_0} - \mathrm{I_t}}{\mathrm{I_0}} \times 100\ (\%)$$

where I_0 is the baseline and I_t is the time-dependent DPV signal. At 48 h, the apical ODI (63.9 ± 4.53%) substantially exceeded the basal ODI (37.7 ± 1.46%), confirming that apical oxygen dynamics are more sensitive to the differentiation-associated metabolic transition. The apical ODI then declined to 47.5 ± 4.73% by 72 h and stabilized, consistent with the signal recovery in Fig. 5e. The oxygen depletion rate (ODR) captures this temporal change as a relative electrochemical rate rather than an absolute flux:

$$\text{Oxygen depletion rate (ODR)} = \frac{\Delta\ \mathrm{ODI}}{\Delta\ \mathrm{t}}$$

The apical ODR shifted from positive to negative between 48 and 72 h. This transition is the central readout of the platform: it marks the change from increasing depletion during proliferation and early differentiation to decreasing depletion during keratinization, mirroring the three-stage metabolic program of Section 2.3—rising consumption at commitment and declining consumption at terminal differentiation. Its timing coincided with the differentiation window defined by marker imaging (K10/filaggrin FPA, Fig. 3b–c), OCR profiling (Fig. 4a–e), and RT-qPCR of both differentiation (K10, involucrin, filaggrin; Fig. 3d) and mitochondrial (MT-CO1, TFAM; Fig. 4f–g) markers, supporting the biological relevance of the signal. The basal ODR, by contrast, showed no negative transition over this interval and crossed toward negative values only after 72 h before stabilizing (Fig. 5f, 5g). This directional lag is mechanistically informative. Basal regions remain proliferative and early-differentiating, and they lie closest to the medium-supplied compartment where oxygen is continuously replenished. Therefore, their depletion declines later and more gradually than that of the apical, air-exposed surface where keratinization concentrates. Bidirectional monitoring thus resolves a spatial gradient of differentiation-associated oxygen dynamics that single-sided sensing cannot capture.

Applying the same analysis across films established biological specificity (Fig. 5g). Differentiation-associated ODR transitions appeared in the GO-Gel-Ca and Gel-Ca groups but not in the Gel or bare-polycarbonate control groups, which lacked the calcium supply required for the metabolic transition. The Gel-Ca transition, however, showed greater signal variability than GO-Gel-Ca, consistent with the less synchronized differentiation documented in Sections 2.2–2.3. The lower variability of GO-Gel-Ca—attributable to GO-mediated calcium immobilization, controlled release, and improved spatial uniformity—indicates that the ODR readout reports not only culture-stage-dependent metabolic changes but also the population-level synchrony of differentiation.

Importantly, basal-side monitoring served as more than a control measurement; it provided a directional reference distinguishing localized differentiation from global metabolic suppression[24,63]. A simultaneous, abrupt decrease from both sides would indicate nonspecific inhibition or loss of viability. The observed apical-dominant transition with a delayed, smaller basal response is incompatible with that scenario and, together with the absence of caspase 3 induction (Section 2.3), rules out cell death as the source of the late-stage signal change.

Collectively, bidirectional ODR monitoring functions as a non-destructive, time-resolved platform for estimating keratinocyte differentiation while preserving the culture structure. The apical ODR transition provides a sensitive functional signature of differentiation-associated metabolic remodeling, and the basal ODR supplies the spatial context for interpreting directional oxygen dynamics. Together they offer a practical, culture-integrated electrochemical approach for tracking keratinocyte differentiation.

3. Conclusion

In this study, we developed a GO-Gel-Ca film-integrated culture and electrochemical monitoring system for non-destructive assessment of keratinocyte differentiation-associated oxygen dynamics. The GO-Gel-

Ca film was designed to function as a transient pore-sealing and calcium-delivery interface on a porous polycarbonate transwell membrane. By combining GO, gelatin, and calcium chloride, the film provided controlled dissolution behavior, gradual calcium release, and improved spatial uniformity of the culture surface. These properties reduced irregular HaCaT aggregation and supported a more synchronized differentiation profile under ALI culture conditions. Image-based marker analysis and RT-qPCR demonstrated that keratinocytes cultured on the GO-Gel-Ca film underwent time-dependent differentiation, characterized by sequential changes in K10, involucrin, and filaggrin expression. Compared with Gel-Ca and control films, the GO-Gel-Ca film produced broader and more uniformly distributed differentiation marker-positive regions, indicating improved spatial reproducibility of keratinocyte differentiation. Seahorse-based OCR and ECAR analysis further showed that differentiation progression was accompanied by culture-stage-dependent metabolic remodeling, comprising a transient rise in glycolytic activity followed by declining mitochondrial respiration and ATP production.

Most importantly, we developed and implemented a bidirectional electrochemical ODR monitoring system that, to our knowledge, is the first to resolve direction-dependent oxygen depletion across a stratifying epithelium within an intact culture. The apical ODR transition between 48 and 72 h provided a functional electrochemical signature of differentiation-associated metabolic remodeling, while basal-side monitoring supplied directional context for distinguishing spatially organized differentiation from global metabolic suppression. This bidirectional design therefore improved the interpretability of oxygen-related electrochemical signals in stratifying keratinocyte cultures.

Overall, the GO-Gel-Ca film-integrated ODR monitoring system provides a practical and minimally invasive approach for tracking keratinocyte differentiation in vitro. By integrating controlled calcium delivery, reduced aggregation, ALI-compatible culture architecture, and apical-basal electrochemical sensing, this system addresses key limitations of endpoint differentiation assays that require fixation or lysis. We note that the ODR reflects a relative electrochemical depletion rate rather than an absolute oxygen flux, and that validation in primary keratinocytes and three-dimensional reconstructed epidermis remains an important future direction. The proposed strategy may nonetheless serve as a useful platform for functional skin model development, epidermal differentiation studies, and future applications in the non-destructive evaluation of barrier-forming epithelial cultures.

Declarations

Acknowledgements

This work was supported by the Nano & Material Technology Development Program through the National Research Foundation of Korea (NRF) grant funded by the Korea government, the Ministry of Science and ICT (MSIT) (Grant No. RS-2024-004104), the National Research Foundation of Korea (NRF) grant funded by the Korea government (MIST) (Grant No. RS-2023-00218543), and Korean ARPA-H Project through the KHIDI, funded by the Ministry of Health & Welfare (Grant No. RS-2024-00512240).

Declaration of interest statement

The authors declare that they have no known competing financial interests that may have influenced the work reported in this paper.

Materials and Methods

Materials

Indium tin oxide (ITO) glass was obtained from U.I.D. (Cheongju, Republic of Korea). Polydimethylsiloxane (PDMS) was purchased from Dow Corning Crop. (Midland, MI, USA). Polycarbonate nanopore film (0.8 μm) was obtained from SPL Life Sciences (Republic of Korea). Graphene oxide water dispersion, gelatin type A powder, calcium chloride ($CaCl_2$), gold chloride trihydrate ($AuCl_3$), Hanks' balanced salt solution (HBSS), phosphate-buffered saline (PBS), foetal bovine serum, and Triton X-100 were purchased from Sigma-Aldrich (Saint Louis, MO, USA). Calcium-free keratinocyte growth medium (KGM) was obtained from Lonza (Walkersville, MD, USA). The HaCaT human keratinocyte cell line was obtained from the KOMA biotechnology (Seoul, Republic of Korea).

Fabrication of the GO-Gel-Ca Film

The GO-Gel-Ca suspension was prepared using distilled water as the solvent. Gelatin type A powder was dissolved in distilled water to prepare gelatin solutions at target concentrations ranging from 0.2 to 20 wt%. Each gelatin solution was mixed with a 20 mg/mL GO suspension at a 1:1 volume ratio, followed by ultrasonication for 30 min to obtain a homogeneous GO-Gel suspension. The final GO concentration in the suspension was fixed at 10 mg/mL, and the pH was maintained between 6.5 and 7.0. Calcium chloride was then added to the GO-Gel suspension to achieve a final calcium ion concentration of 1.6 mM. After the addition of calcium chloride, the suspension was further ultrasonicated for 60 min to promote uniform dispersion and interaction among GO, gelatin, and calcium ions. The resulting GO-Gel-Ca suspension was deposited onto polycarbonate film at 25 μL per 25 mm^2 area. The coated films were spin-coated at 500 rpm for 5 min to form a uniform GO-Gel-Ca layer on the polycarbonate substrate. After spin coating, the GO-Gel-Ca films were dried at room temperature for 24 h before use. Prior to cell culture experiments, the fabricated films were integrated into cell culture cartridges using PDMS-based bonding.

Characterization of the GO-Gel-Ca Film

The GO-Gel-Ca film was characterized to confirm GO coating, calcium incorporation, pore sealing, surface morphology, and calcium release behavior. Energy-dispersive X-ray spectroscopy (EDS) was used to analyze the distribution of Ca and Cl ions on the film surface. Scanning electron microscopy (SEM) was performed to evaluate pore sealing and surface morphology of the coated polycarbonate film. Raman spectroscopy was used to confirm the presence and spatial distribution of GO on the film. For D/G ratio mapping, Raman spectra were processed by Gaussian fitting to extract the relative intensities of the D and G bands. The resulting D/G ratio maps were used to assess the distribution of GO across the coated surface and pore-sealed regions. Calcium release from the GO-Gel-Ca film was

quantified using inductively coupled plasma optical emission spectroscopy (ICP-OES). To minimize interference from medium components, calcium release was measured in distilled water rather than in culture medium. The released calcium concentration was analyzed as a function of exposure time and, when applicable, exposure direction.

Fabrication of the GO-Gel-Ca Film Cartridge-Integrated Bidirectional Electrochemical System

Gold nanostructure-based working electrodes were fabricated on ITO glass substrates. Prior to electrode fabrication, the ITO glass was sequentially washed with 1% Triton X-100 solution, distilled water, and 70% ethanol. A cartridge-fixing chamber was assembled onto the ITO glass using PDMS. Gold was deposited onto the ITO glass within the cartridge-fixing chamber using a 5 mM $AuCl_3$ solution. The gold-deposited ITO glass samples were subsequently annealed at 70 °C for 3 h. The resulting gold nanostructure-based working electrodes integrated with the cartridge-fixing chambers were used in combination with platinum-based reference and counter electrodes. For bidirectional electrochemical measurements, the GO-Gel-Ca film cartridge was positioned between two gold nanostructure-based working electrodes, enabling independent electrochemical monitoring from both sides of the cartridge.

Cell Culture

HaCaT cells were cultured on conventional cell culture plates and on cartridge-integrated transwell platforms at 37 °C in a humidified atmosphere containing 5% CO_2. The cell culture medium consisted of KBM supplemented with 10% FBS, 0.4% bovine pituitary extract, 0.01% human epidermal growth factor, 0.01% insulin, 0.01% hydrocortisone, and 0.01% gentamicin sulfate-amphotericin. The culture medium was replaced every 24 h. Experiments performed outside the incubator were conducted at 25 °C. The number of keratinocytes seeded on each platform was fixed at 15,000 cells under all conditions.

Image-Based Analysis of Differentiation Marker Expression

The expression of four keratinocyte differentiation-related markers, K14, K10, IVL, and FLG, was analyzed using fluorescence images acquired by confocal microscopy (TCS SP8; Leica Microsystems, Wetzlar, Germany). For all samples, z-stack images were acquired at 1 μm intervals to enable three-dimensional image-based analysis of marker distribution. All fluorescence images were preprocessed using identical thresholding conditions. Images were binarized using a gray value threshold of 160 on an 8-bit scale ranging from 0 to 255, and the same preprocessing parameters were applied consistently to all images. Marker-positive regions were quantified based on the binarized fluorescence images. Imaging was performed using Application Suite X (Leica Microsystems). Excitation and emission wavelength scans were obtained by scanning the excitation spectrum of the sample while simultaneously recording the fluorescence emission spectrum at each excitation wavelength.

RT -qPCR Analysis

Gene expressions associated with keratinization and metabolic activity were evaluated by reverse transcription quantitative polymerase chain reaction (RT-qPCR) (Table S1). Briefly, adherent cells were

lysed in RLT buffer containing 20 mM β-mercaptoethanol, and total RNA was extracted from the lysates using an RNA extraction kit (QIAGEN GmbH; Germany) according to the manufacturer's protocol. Complementary DNA (cDNA) was synthesized using a cDNA synthesis kit (TAKARA BIO INC.; Japan). RT-RT-qPCR was subsequently performed using the synthesized cDNA to quantify the expression of target genes. GAPDH expression was used as an internal housekeeping control for normalization.

Evaluation of oxygen consumption rate

Cells cultured on GO-Gel-Ca films were detached from the film by repeated exposure to trypsin-EDTA at 3 min intervals for 2–3 cycles. The detached cells were collected and seeded into XF96 plates at densities yielding approximately 80–90% confluency, followed by overnight incubation at 37 °C in a humidified atmosphere containing 5% CO_2. Mitochondrial function was evaluated using the Seahorse XF Cell Mito Stress Test Kit (Agilent) according to the manufacturer's protocol. On the day of the assay, cells were washed twice with pre-warmed XF assay medium consisting of base medium supplemented with 10 mM glucose and 2 mM L-glutamine. The cells were then equilibrated for 45 min in a non-CO_2 incubator. Sensor cartridges were pre-hydrated overnight at 37 °C under non-CO_2 conditions. Oligomycin (1.5 μM), FCCP (1.0 μM), and rotenone/antimycin A (0.5 μM) were prepared in assay medium and loaded into ports A, B, and C, respectively. The assay was performed using a Seahorse XF Analyzer with sequential compound injections to derive mitochondrial respiration parameters, including basal respiration, ATP-linked respiration, maximal respiration, and spare respiratory capacity. Data were analyzed using Wave software and normalized to cell counts or protein content.

Immunocytochemistry Analysis

For immunocytochemical staining, cells were washed with 1× PBS (pH 7.4) and fixed with 4% formaldehyde for 30 min. The fixed cells were permeabilized with 3% Triton X-100 diluted in 1× PBS for 30 min and washed twice with 1× PBS. Nuclei were counterstained with Hoechst 33342 (Thermo Scientific, Germany) for 30 min. Fixed cells were stained with Alexa Fluor® 488 Anti-Cytokeratin 14 antibody, Alexa Fluor® 647 Anti-Cytokeratin 10 antibody, involucrin polyclonal antibody, and filaggrin polyclonal antibody (Thermo Scientific, Germany) for 60 min at room temperature (25 °C). After staining, samples were washed with PBS and imaged using confocal microscopy for subsequent marker expression and fluorescence-positive area analysis.

Electrochemical monitoring

Differential pulse voltammetry (DPV) was performed using a DY2000 series multi-channel potentiostat (Digi-Ivy). Ag/AgCl (1 M KCl) and platinum wire were used as the reference and counter electrodes, respectively. Gold nanostructures deposited on ITO glass were used as the working electrodes. Prior to electrochemical measurement, the growth medium was removed and replaced with oxygen-calibrated HBSS. DPV measurements were performed over a voltage range of −0.5 to 0 V, with a step voltage of 0.005 V, sensitivity of 1.0×10^{-5}, and sampling time of 0.02 s. Oxygen calibration of HBSS was performed using the same DPV detection procedure. Briefly, 50 mL of HBSS was purged with nitrogen for 10–30

min, and HBSS samples that produced a DPV current within the range of 80 ± 2 μA at −0.3 V were used for subsequent detection. DPV measurements from the apical and basal directions were performed independently. For each measurement, freshly calibrated HBSS was used to minimize variation in baseline oxygen-related electrochemical signals. The resulting DPV responses were used to analyze oxygen-related electrochemical changes associated with keratinocyte culture time and sensing direction.

References

1. Moreci, R. S. & Lechler, T. Epidermal structure and differentiation. *Current Biology* 30, R144–R149 (2020).
2. Simpson, C. L., Patel, D. M. & Green, K. J. Deconstructing the skin: cytoarchitectural determinants of epidermal morphogenesis. *Nature reviews Molecular cell biology* 12, 565–580 (2011).
3. Harris-Tryon, T. A. & Grice, E. A. Microbiota and maintenance of skin barrier function. *Science* 376, 940–945 (2022).
4. Pat, Y. *et al.* Effect of altered human exposome on the skin and mucosal epithelial barrier integrity. *Tissue Barriers* 11, 2133877 (2023).
5. Lecomte, K., Toniolo, A. & Hoste, E. Cell death as an architect of adult skin stem cell niches. *Cell Death & Differentiation* 31, 957–969 (2024).
6. Blanpain, C. & Fuchs, E. Epidermal homeostasis: a balancing act of stem cells in the skin. *Nature reviews Molecular cell biology* 10, 207–217 (2009).
7. Mikesell, A. R. *et al.* Increased keratinocyte activity and PIEZO1 signaling contribute to paclitaxel-induced mechanical hypersensitivity. *Science Translational Medicine* 16, eadn5629 (2024).
8. Cho, Y. *et al.* NLRP10 maintains epidermal homeostasis by promoting keratinocyte survival and P63-dependent differentiation and barrier function. *Cell death & disease* 15, 759 (2024).
9. Alinezhad, V. *et al.* Engineering a platelet-rich plasma-based multifunctional injectable hydrogel with photothermal, antibacterial, and antioxidant properties for skin regeneration. *Biomaterials Science* 11, 5872–5892 (2023).
10. Hosseini, M. & Shafiee, A. Engineering bioactive scaffolds for skin regeneration. *Small* 17, 2101384 (2021).
11. Na, Y., Kim, Y., Lee, J. H. & Sung, G. Y. Fabrication of a Contraction-Free Full-Thickness Human Skin Equivalent Using Skin-on-a-Chip with Silk Fibroin Scaffold. *BioChip Journal* 19, 849–858 (2025).
12. Park, J. Y. *et al.* TASL mediates keratinocyte differentiation by regulating intracellular calcium levels and lysosomal function. *Scientific Reports* 14, 10978 (2024).
13. Tian, M. *et al.* Drug evaluation platform based on non-destructive and real-time in situ organoid fate state monitoring by graphene field-effect transistor. *Chemical Engineering Journal* 498, 155355 (2024).
14. Sekine, O. *et al.* Seamless and non-destructive monitoring of extracellular microRNAs during cardiac differentiation from human pluripotent stem cells. *Stem cell reports* 18, 1925–1939 (2023).

15. Ahn, J. *et al.* Modeling of three-dimensional innervated epidermal like-layer in a microfluidic chip-based coculture system. *Nature communications* 14, 1488 (2023).
16. Gareus, R. *et al.* Normal epidermal differentiation but impaired skin-barrier formation upon keratinocyte-restricted IKK1 ablation. *Nature cell biology* 9, 461–469 (2007).
17. Jung, K. L. *et al.* Single-cell analysis of Kaposi's sarcoma-associated herpesvirus infection in three-dimensional air-liquid interface culture model. *PLoS Pathogens* 18, e1010775 (2022).
18. Frankart, A. *et al.* Epidermal morphogenesis during progressive in vitro 3 D reconstruction at the air–liquid interface. *Experimental dermatology* 21, 871–875 (2012).
19. Shen, X. *et al.* Keratinocyte-specific H4K12 lactylation drives a non-canonical IL-17-dependent signaling in psoriasis progression in mice. *Nature Communications* 16, 8639 (2025).
20. Taguchi, S. *et al.* Overexpression of the transcription factor Yin-Yang-1 suppresses differentiation of HaCaT cells in three-dimensional cell culture. *Journal of investigative dermatology* 131, 37–45 (2011).
21. Roshan, A. *et al.* Human keratinocytes have two interconvertible modes of proliferation. *Nature cell biology* 18, 145–156 (2016).
22. Koo, K. M. *et al.* Extracellularly detectable electrochemical signals of living cells originate from metabolic reactions. *Advanced Science* 10, 2207084 (2023).
23. Koo, K.-M. *et al.* Electrochemical platform for in situ metabolic profiling and therapeutic evaluation of triple-negative breast cancer. *Chemical Engineering Journal*, 173253 (2026).
24. Haensel, D. *et al.* Defining epidermal basal cell states during skin homeostasis and wound healing using single-cell transcriptomics. *Cell reports* 30, 3932–3947. e3936 (2020).
25. Zhang, Z. *et al.* Differential glucose requirement in skin homeostasis and injury identifies a therapeutic target for psoriasis. *Nature medicine* 24, 617–627 (2018).
26. Prak, K. *et al.* Functional analyses and integrated mechanisms of cellular destruction by L-amino acid oxidase. *Cell Death & Disease* (2025).
27. Wickersham, M. *et al.* Metabolic stress drives keratinocyte defenses against Staphylococcus aureus infection. *Cell reports* 18, 2742–2751 (2017).
28. Cho, Y. *et al.* Sensing Modalities Across the Biological Hierarchy From Single Cells to Organs for Cellular Efflux Monitoring. *Advanced Functional Materials*, e31976 (2026).
29. Lin, Y., Trouillon, R., Safina, G. & Ewing, A. G. Chemical analysis of single cells. *Analytical Chemistry* 83, 4369–4392 (2011).
30. Yang, J., Deng, S., Lei, J., Ju, H. & Gunasekaran, S. Electrochemical synthesis of reduced graphene sheet–AuPd alloy nanoparticle composites for enzymatic biosensing. *Biosensors and Bioelectronics* 29, 159–166 (2011).
31. Cheng, M.-H., Chicco, A. J., Ball, D. & Chen, T. W. Analysis of mitochondrial oxygen consumption and hydrogen peroxide release from cardiac mitochondria using electrochemical multi-sensors. *Sensors and Actuators B: Chemical* 360, 131641 (2022).

32. Hiramoto, K. *et al.* Development of oxygen consumption analysis with an on-chip electrochemical device and simulation. *Analytical chemistry* 89, 10303–10310 (2017).
33. Nielsen, L. P., Risgaard-Petersen, N., Fossing, H., Christensen, P. B. & Sayama, M. Electric currents couple spatially separated biogeochemical processes in marine sediment. *Nature* 463, 1071–1074 (2010).
34. Koo, K.-M., Wi, J.-K., Kim, C.-D., Kim, H.-J. & Kim, T.-H. Cell-based electrochemical biosensors for cancer diagnosis: Advances and emerging trends. *TrAC Trends in Analytical Chemistry*, 118669 (2026).
35. Clark, R. B. & Dick, J. E. Electrochemical sensing of perfluorooctanesulfonate (PFOS) using ambient oxygen in river water. *ACS sensors* 5, 3591–3598 (2020).
36. Zhong, X. *et al.* Spatially and temporally resolved dynamic response of Co-based composite interface during the oxygen evolution reaction. *Journal of the American Chemical Society* 146, 7467–7479 (2024).
37. Li, J. *et al.* Mechanistic Insights into NO2 Sensing at Room Temperature: Oxygen Vacancy Dynamics Revealed by in Situ Optoelectronic Characterization. *Nano Letters* (2026).
38. Kim, C.-H., Ju, F. N., Kim, C.-D., Son, H. & Kim, T.-H. Enhanced sphericity and uniformity in adenocarcinoma spheroids on chip via fibroblast co-culture for electrochemical drug screening. *Chemical Engineering Journal* 512, 162547 (2025).
39. Wang, H. *et al.* NIR-II AIE luminogen-based erythrocyte-like nanoparticles with granuloma-targeting and self-oxygenation characteristics for combined phototherapy of tuberculosis. *Advanced Materials* 36, 2406143 (2024).
40. Chen, Q., Kim, J., Choi, M. & Jeon, S. Advancing solar energy applications with graphene: the potential of minimally oxidized graphene. *Nano Convergence* 12, 30 (2025).
41. Kim, C. H. *et al.* Fabrication of Free-Standing Undulating Graphene Oxide Modular Tapered Pipes Using the Marangoni Effect. *Advanced Functional Materials* 35, 2512291 (2025).
42. Wells, M. P. *et al.* Novel electrostatic dry lift-off and transfer route for vertically aligned nanocomposite oxide thin films. *Nano Convergence* 12, 37 (2025).
43. Lee, M.-J. *et al.* Nanoparticle-functionalized organoid-on-a-chip systems for biomedical applications. *BioChip Journal* 19, 386–410 (2025).
44. Bellier, N., Baipaywad, P., Ryu, N., Lee, J. Y. & Park, H. Recent biomedical advancements in graphene oxide-and reduced graphene oxide-based nanocomposite nanocarriers. *Biomaterials research* 26, 65 (2022).
45. Zhai, H. *et al.* Spatially guided construction of multilayered epidermal models recapturing structural hierarchy and cell–cell junctions. *Small Science* 2, 2200051 (2022).
46. Zhai, H. *et al.* 3D organotypic skin models recapitulate autoantibody-driven pemphigus pathomechanisms and targeted therapeutic response. *Science Advances* 12, eadz5003 (2026).

47. Zhang, Z. *et al.* Activation of unfolded protein response pathways promotes keratinocyte differentiation and ameliorates psoriasis phenotypes. *Cell Stress and Chaperones*, 100163 (2026).
48. Zheng, S., Wang, X., Zhao, D., Liu, H. & Hu, Y. Calcium homeostasis and cancer: insights from endoplasmic reticulum-centered organelle communications. *Trends in cell biology* 33, 312–323 (2023).
49. Feng, Y. *et al.* A bioinspired gelatin–amorphous calcium phosphate coating on titanium implant for bone regeneration. *Advanced Healthcare Materials* 12, 2203411 (2023).
50. Fabbri, R. *et al.* Graphene oxide electrodes enable electrical stimulation of distinct calcium signalling in brain astrocytes. *Nature nanotechnology* 19, 1344–1353 (2024).
51. Anegbe, B., Ifijen, I. H., Maliki, M., Uwidia, I. E. & Aigbodion, A. I. Graphene oxide synthesis and applications in emerging contaminant removal: a comprehensive review. *Environmental Sciences Europe* 36, 15 (2024).
52. Jafarian, H. *et al.* Synthesis of heterogeneous metal organic Framework-Graphene oxide nanocomposite membranes for water treatment. *Chemical Engineering Journal* 455, 140851 (2023).
53. Frontinan-Rubio, J., Gomez, M. V., González, V. J., Durán-Prado, M. & Vázquez, E. Sublethal exposure of small few-layer graphene promotes metabolic alterations in human skin cells. *Scientific Reports* 10, 18407 (2020).
54. Wang, F. *et al.* Loss of TACSTD2 contributed to squamous cell carcinoma progression through attenuating TAp63-dependent apoptosis. *Cell death & disease* 5, e1133–e1133 (2014).
55. Malak, M. *et al.* Insights into metabolic changes during epidermal differentiation as revealed by multiphoton microscopy with fluorescence lifetime imaging. *Scientific Reports* 15, 6377 (2025).
56. Hamanaka, R. B. & Chandel, N. S. Mitochondrial metabolism as a regulator of keratinocyte differentiation. *Cellular logistics* 3, ra8 (2013).
57. Simpson, C. L. *et al.* NIX initiates mitochondrial fragmentation via DRP1 to drive epidermal differentiation. *Cell reports* 34 (2021).
58. Porter, A. G. & Jänicke, R. U. Emerging roles of caspase-3 in apoptosis. *Cell death & differentiation* 6, 99–104 (1999).
59. Ma, X. *et al.* Mechanisms and applications of manganese-based nanomaterials in tumor diagnosis and therapy. *Biomaterials Research* 29, 0158 (2025).
60. Bikle, D. D., Xie, Z. & Tu, C.-L. Calcium regulation of keratinocyte differentiation. *Expert review of endocrinology & metabolism* 7, 461–472 (2012).
61. Deng, W. *et al.* A fully integrated wearable biomimetic microfluidic wound tracker for in situ dynamic monitoring of wound exudate oxygen. *ACS nano* 19, 16163–16174 (2025).
62. Chang, B. *et al.* Dynamic redox induced localized charge accumulation accelerating proton exchange membrane electrolysis. *Advanced Materials* 37, 2405447 (2025).
63. Ochiai-Noguchi, M., Horikoshi, A., Hirakata, S. & Yoshihara, T. Visualization of oxygen profile in reconstructed human epidermis by phosphorescence-lifetime imaging microscopy using Ir (III)

complex. *Scientific Reports* 15, 36008 (2025).

Figures

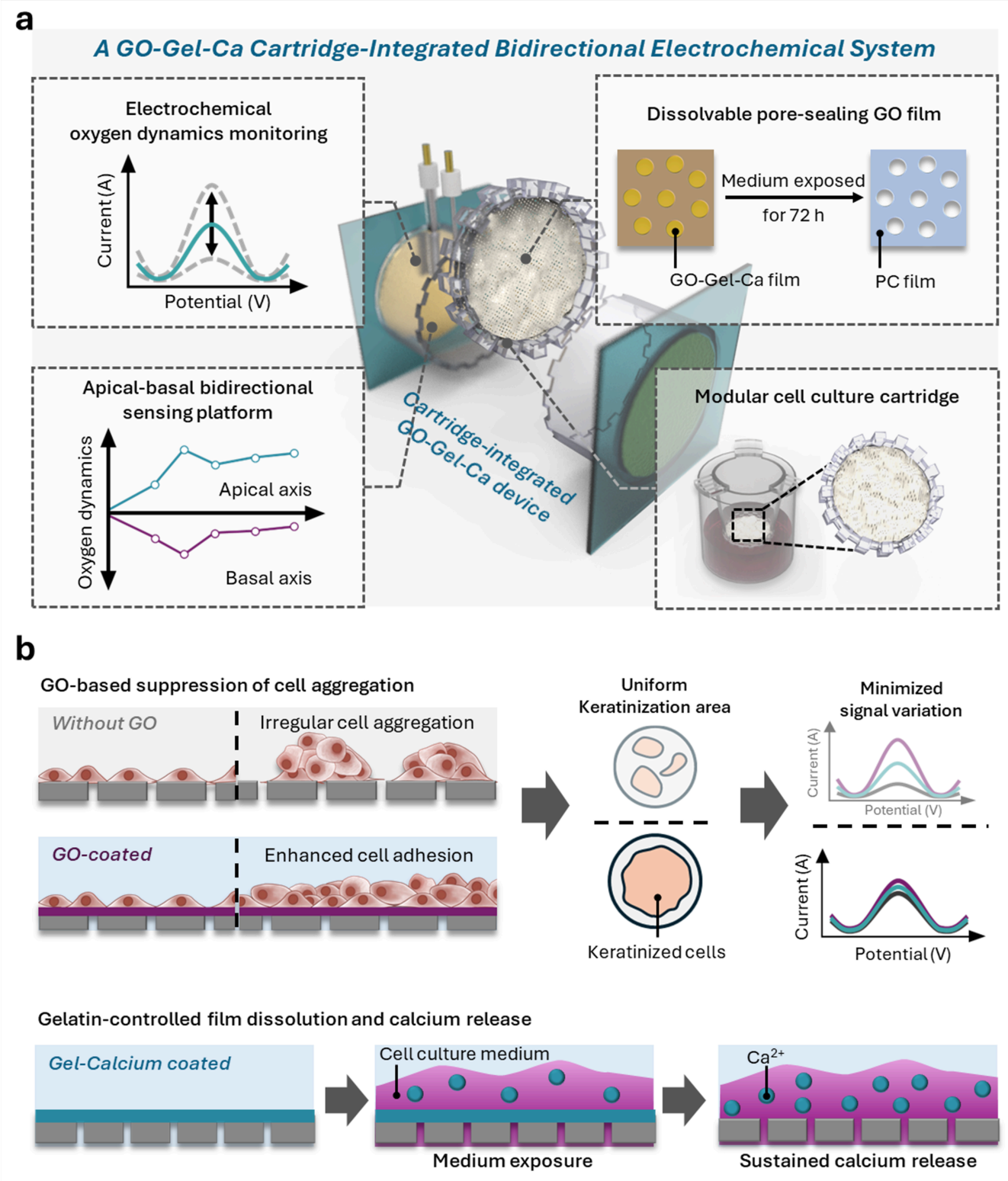

Figure 1

Schematic representation of the GO-Gel-Ca film cartridge-integrated bidirectional electrochemical system. (a) Overview of the GO-Gel-Ca film-integrated bidirectional electrochemical system. (b) Schematic illustration showing the functional features of the GO-Gel-Ca film.

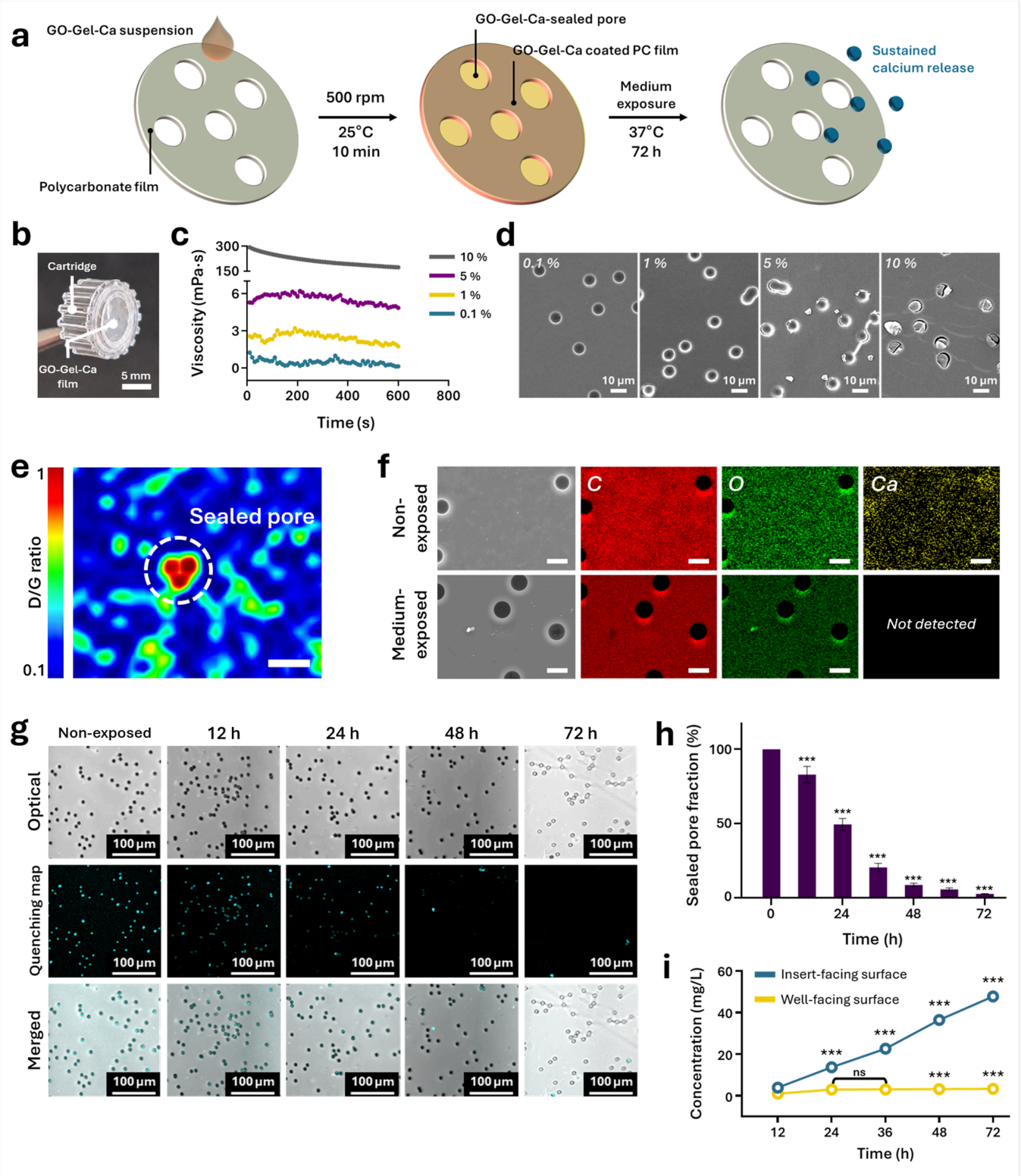

Figure 2

Fabrication process and calcium release properties of the GO-Gel-Ca film. (a) Schematic illustration of the GO-Gel-Ca film fabrication process and calcium release mechanism. (b) Optical image of the cartridge-type GO-Gel-Ca film. (c) Viscosity of the GO-Gel-Ca suspension as a function of gelatin concentration and (d) representative surface SEM images. (e) Raman spectroscopy-based D/G ratio mapping image of the film surface. The region inside the white dashed line indicates pores sealed by the GO-Gel-Ca film. (f) SEM-EDS analysis of residual calcium within the film before and after exposure to culture medium. (g) Quantitative analysis of the number of sealed pores according to culture medium exposure time, based on optical and fluorescence-quenching images. (h) Quantitative pore reopening analysis of transiently sealed pores during incubation. The sealed pore fraction was defined as the proportion of fluorescence-quenched pores relative to the total number of pores observed in the image. (i) ICP-OES-based analysis of calcium release from the film according to exposure time and exposure direction in distilled water. Student's t-test, n = 5, *p < 0.05, **p < 0.01, ***p < 0.001. Scale bar = 10 μm.

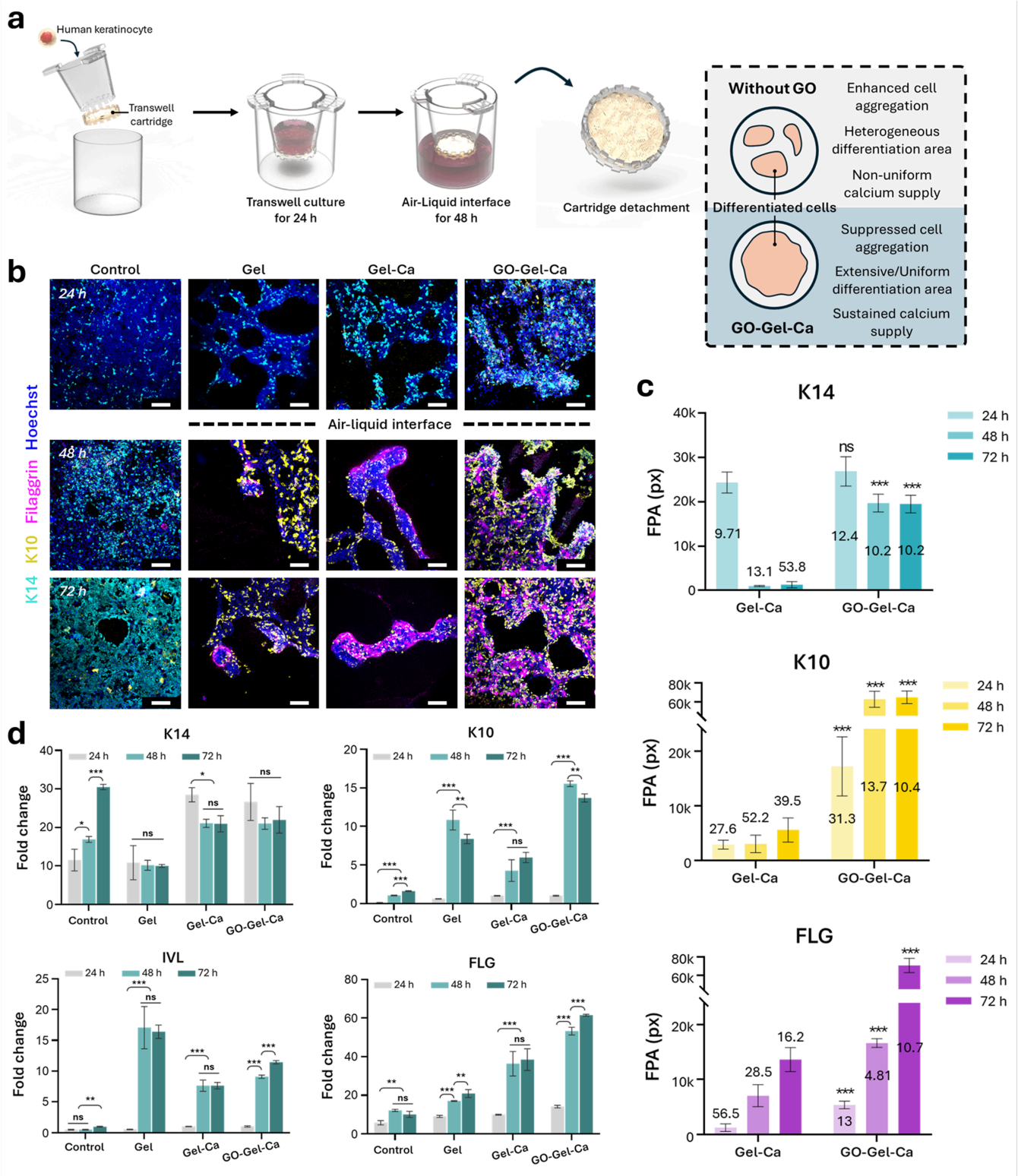

Figure 3

Computational image analysis and RT-qPCR analysis for evaluating keratinocyte differentiation. (a) Schematic illustration showing the cell culture cartridge incorporating the GO-Gel-Ca film and its culture configuration. (b) Fluorescence images of keratinocytes cultured on the cartridge and stained for Keratin 14 (K14), Keratin 10 (K10), filaggrin (FLG), and Hoechst. (c) Culture time-dependent fluorescence-positive area (FPA) of K14-, K10-, and FLG-positive keratinocytes quantified by computational image analysis. The

values inserted above the graphs indicate the coefficient of variation (CV), defined as the ratio of the standard deviation to the mean. (d) RT-qPCR-based analysis of culture time-dependent expression levels of K14, K10, involucrin (IVL), and FLG in keratinocytes. Student's t-test, n = 7, *p < 0.05, **p < 0.01, ***p < 0.001. ns indicates not significant. Scale bar = 50 μm.

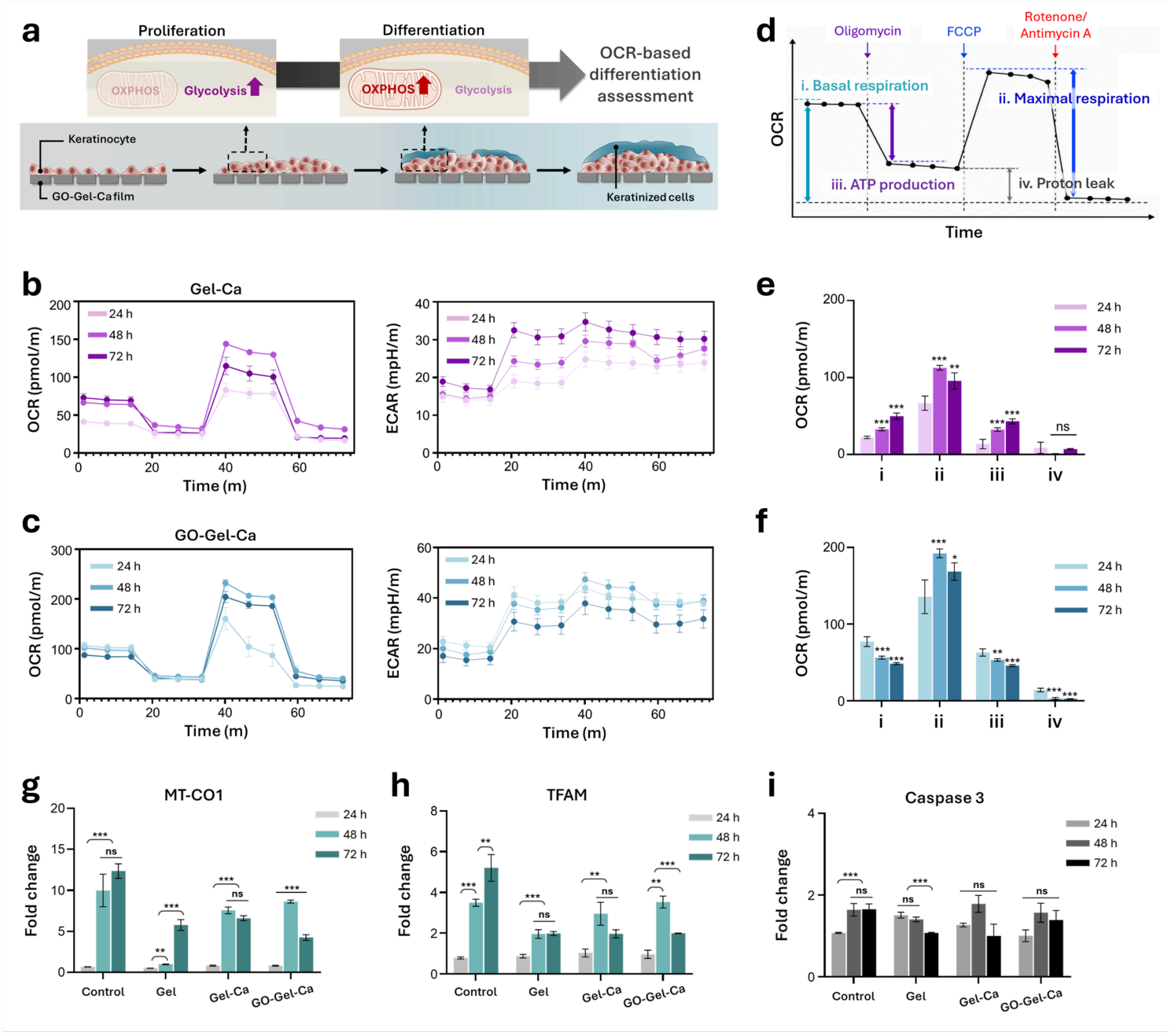

Figure 4

Analysis of keratinocyte oxygen dynamics based on oxygen consumption rate. (a) Schematic illustration showing keratinocyte differentiation monitoring using oxygen consumption rate (OCR) analysis. (b and c) Culture time-dependent OCR and extracellular acidification rate (ECAR) profiles of keratinocytes cultured on (b) Gel-Ca films and (c) GO-Gel-Ca films. (d) Seahorse XF-based OCR assay profile. (e and f) Detailed OCR parameter analysis of keratinocytes cultured on (e) Gel-Ca films and (f)

GO-Gel-Ca films. Roman numerals on the x-axis correspond to the test stages indicated in the profile shown in (d). (g–i) RT-qPCR-based analysis of culture time-dependent expression levels of mitochondrially encoded cytochrome C oxidase I (MT-CO1), mitochondrial transcription factor A (TFAM), and caspase-3 in keratinocytes. Student's t-test, n = 5, *p < 0.05, **p < 0.01, ***p < 0.001. ns indicates not significant.

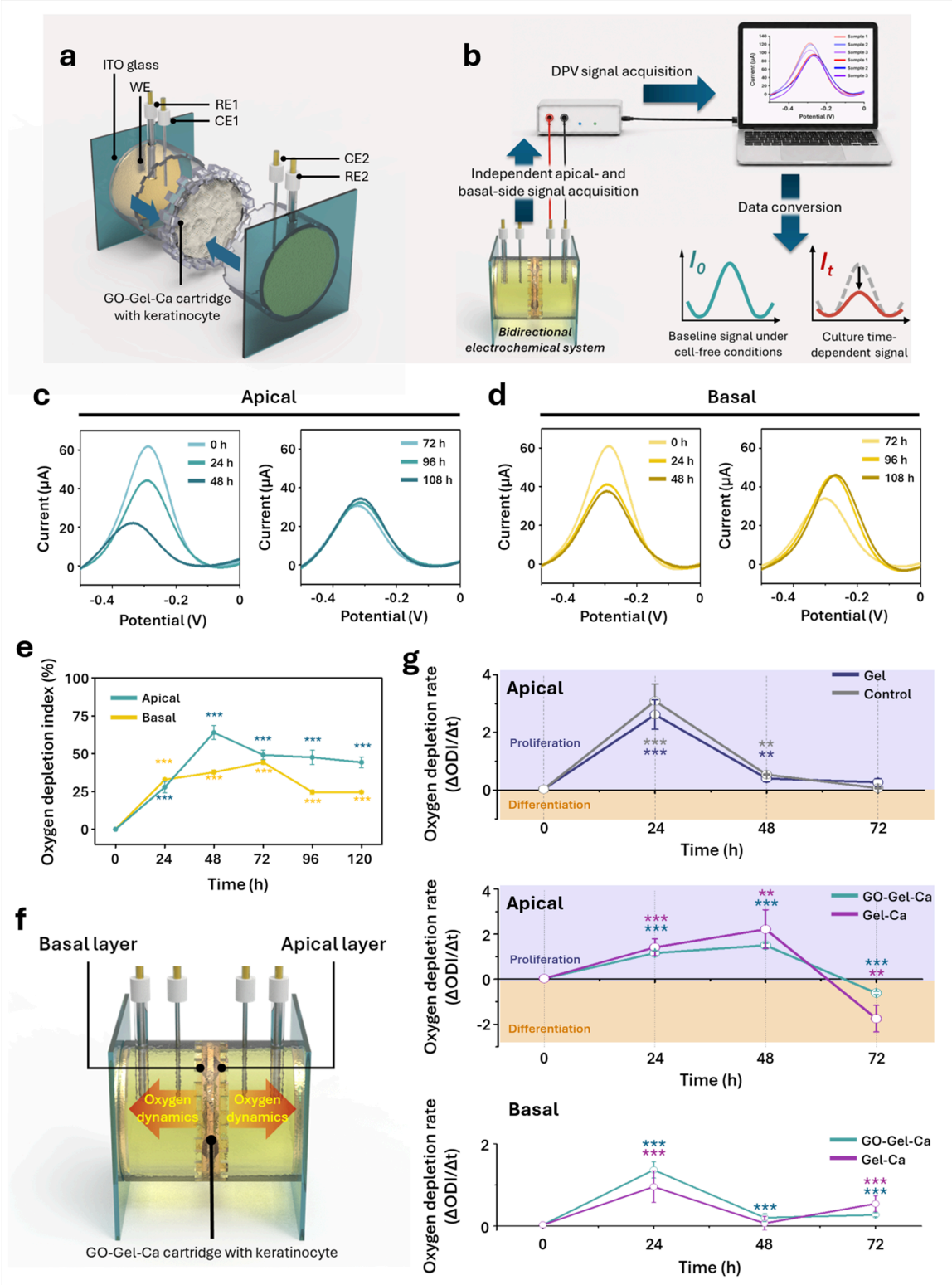

Figure 5

Time-dependent keratinocyte differentiation monitoring using the GO-Gel-Ca film-integrated bidirectional electrochemical system. (a) Schematic illustration showing the structure of the GO-Gel-Ca film-integrated bidirectional electrochemical system and (b) data derivation process based on the system. (c) DPV-based electrochemical analysis of oxygen dynamics according to culture time from the apical side of keratinocytes, corresponding to the insert-facing (apical) side of the GO-Gel-Ca film, and the basal side, corresponding to the well-facing side of the film (d). (e) Oxygen depletion index according to the sensing position of the GO-Gel-Ca film. (f) Schematic illustration showing the operating principle of the bidirectional electrochemical system. (g) Oxygen depletion rate analysis according to sensing position and GO-Gel-Ca film fabrication condition. Student's t-test, n = 5, *p < 0.05, **p < 0.01, ***p < 0.001. ns indicates not significant.

Supplementary Files

This is a list of supplementary files associated with this preprint. Click to download.

- SIKeratinizationmonitoring260608.docx